Domain Size of Phase-Separated Na$_x$CoO$_2$ as Investigated by X-Ray Microdiffraction

Hideharu Niwa [1,2,*], Takayuki Shibata [1,3], Yasuhiko Imai [4], Shigeru Kimura [4] and Yutaka Moritomo [1,2,*]

[1] Faculty of Pure and Applied Science, University of Tsukuba, Tsukuba 305-8571, Japan; shibata@nat.gunma-ct.ac.jp
[2] Center for Integrated Research in Fundamental Science and Engineering (CiRfSE), University of Tsukuba, Tsukuba 305-8571, Japan
[3] National Institute of Technology, Gunma College, Gunma 371-8530, Japan
[4] Japan Synchrotron Radiation Research Institute (JASRI), Kouto, Sayo 679-5198, Japan; imai@spring8.or.jp (Y.I.); kimuras@spring8.or.jp (S.K.)
[*] Correspondence: niwa.hideharu.ga@u.tsukuba.ac.jp (H.N.); moritomo.yutaka.gf@u.tsukuba.ac.jp (Y.M.); Tel.: +81-29-853-4216 (H.N.); +81-29-853-4337 (Y.M.)

Abstract: O3-NaCoO$_2$ is a promising cathode material for sodium ion secondary batteries (SIBs). Na$_x$CoO$_2$ shows phase separation (PS) into the O3 and O'3 phases in the Na concentration range of $0.89 \leqslant x \leqslant 0.99$. In order to estimate the domain size (r) in the two-phase region, we performed X-ray microdiffraction (XRMD) of thin films of Na$_x$CoO$_2$ at $x = 0.97$ and ~ 1. We found that r ($\approx$400 nm) of the O'3 domain is comparable to the particle size d ($=331 \pm 87$ nm) in the as-grown O3-NaCoO$_2$ film. This observation suggests that individual particles of Na$_x$CoO$_2$ are single phase to minimize the strain at the O3–O'3 phase boundary.

Keywords: secondary batteries (SIBs); thin film of O3-NaCoO$_2$; X-ray microdiffraction (XRMD)

1. Introduction

Sodium ion secondary batteries (SIBs) store electric energy by the intercalation/deintercalation of abundant Na$^+$ (Clark number = 2.63) [1,2]. In this sense, SIBs are suitable for large-scale batteries for the stable use of solar and wind energies. Recently, Komaba et al. [3] reported that hard carbon shows a good discharge capacity ($\geqslant$200 mAh/g) and cyclability as an anode for SIB. This observation has stimulated the development of SIBs for commercial utilization. Among the cathode materials for SIBs, layered oxides (NaMO$_2$, where M is a transition metal) with O3-type structure shows promising electrochemical properties [4–6]. For example, O3-NaCrO$_2$ [4] shows a capacity of 120 mAh/g and an average operating voltage of 3.0 V with good cyclability. In addition, O3-NaFe$_{1/2}$Co$_{1/2}$O$_2$ [5] shows a capacity of 160 mAh/g and an average operating voltage of 3.1 V with good cyclability.
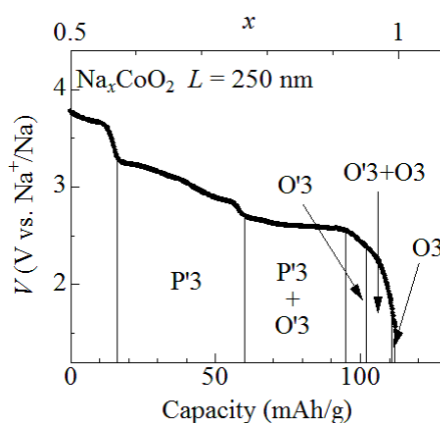
Most of the O3-type materials, however, show successive phase transitions and phase separations (PSs). For example, O3-NaCoO$_2$ shows successive phase transitions with decreases in the Na concentration (x) [7,8]: O3 ($0.99 \leqslant x \leqslant 1$), O3 + O'3 ($0.89 \leqslant x \leqslant 0.99$), O'3 ($0.81 \leqslant x \leqslant 0.89$), O'3 + P'3 ($0.68 \leqslant x \leqslant 0.81$), and P'3 ($0.59 \leqslant x \leqslant 0.68$). The O3 phase belongs to trigonal structure ($R\bar{3}m$; $Z = 3$) with the AB|CA|BC stacking of the oxygen sheets, while the O'3 phase belongs to monoclinic structure ($C2/m$; $Z = 2$) with the same oxygen stacking. On the other hand, the P'3 phase belongs to hexagonal structure ($P6_3/mmc$; $Z = 2$) with the modified AB|BC|CA oxygen stacking. These structural changes seriously influence the cyclability and rate properties of the batteries.

In this paper, we investigated domain size (r) of the O′3 phase in the O3–O′3 phase-separated Na_xCoO_2 by means of X-ray microdiffraction (XRMD). We concentrated our attention to the O3 + O′3 region ($0.89 \leqslant x \leqslant 0.99$), because the oxygen stacking remains the same. We found that r ($\approx$400 nm) of the O′3 domain is comparable to the particle size d (=331 ± 87 nm) in the as-grown O3-NaCoO$_2$ film. This observation suggests that individual particles of Na_xCoO_2 are single phase to minimize the strain at the O3–O′3 phase boundary.

2. Results

2.1. Discharge Curve of O3-NaCoO$_2$ Film

Figure 1 shows discharge curves of the O3-NaCoO$_2$ film measured at 1.6C. The observed capacity (=112 mAh/g) is close to the ideal value (=113 mAh/g) of Na_xCoO_2. With use of the ideal capacity, we converted the discharge capacity into x and plotted the value on the upper axis. The capacity of the O3-NaCoO$_2$ film slightly decreases with increase in the discharge rate, even at $\sim$1C [9]: 116 mAh/g at 0.2C, 100 mAh/g at 1.2C, and 82 mAh/g at 12C. Then, the x value may be slightly overestimated. Lei et al. [7] and Delmas et al. [8] investigated successive phase transitions of Na_xCoO_2 and determined single- and two-phase regions against x. For convenience of the explanation, the single- and two-phase regions are cited from reference [7].
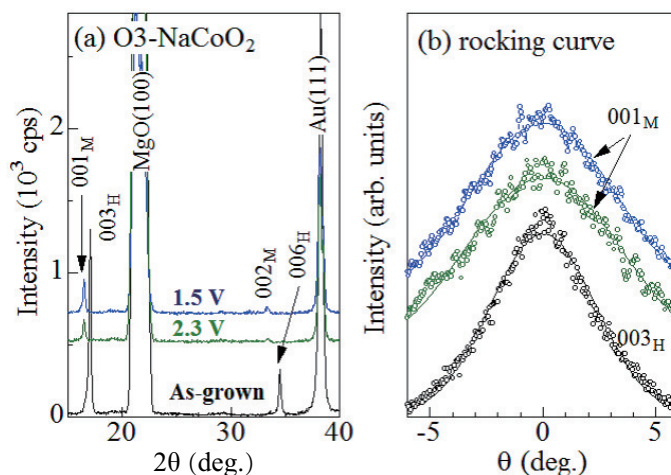

Figure 1. Discharge curves of the O3-NaCoO$_2$ film measured at 1.6C. The film thickness (L) is 250 nm. O3, O′3, and P′3 represented structural phases (cited from reference [7]).

2.2. X-Ray Diffraction and Rocking Curve

Figure 2a shows X-ray diffraction (XRD) patterns of the as-grown, 2.3 V, and 1.5 V films. The X-ray source was the Cu Kα line (λ = 1.54 Å) operated at 40 kV and 40 mA. The 2.3 V and 1.5 V films locate in the O3 single phase region and O3 + O′3 two-phase region: their x values are 0.97 and $\sim$1, respectively (Figure 1). In the as-grown film, intense 003$_H$ and 006$_H$ reflections are observed, indicating the 001-orientation of the films. We confirmed that the lattice constant c (=15.6 Å) of the as-grown film is consistent with the value (=15.58698(11) Å [9]) of the O3 phase. In the 2.3 V and 1.5 V films, the corresponding reflections shift to the low-2θ side, indicating widening of the interlayer distance. The interlayer distance ($\approx$5.37 Å) is close to the value ($\approx$5.35 Å [7]) of the O′3 phase. Therefore, we assigned the $\sim$16.5° (33.0°) reflections to 001$_M$ [002$_M$] of the O′3 phase. We note that no trace of the 003$_H$ and 006$_H$ reflections are observed in the 2.3 V and 1.5 V films, indicating that the films are dominated by the O′3 phase.

In order to investigate the out-of-plane distribution of the crystal orientation, we measured the out-of-plane rocking curves. Figure 2b shows the rocking curves at the 003$_H$, 001$_M$, and 001$_M$ reflections of the as-grown, 2.3 V, and 1.5 V films, respectively. Full width of half maxima (FWHM) are 5.5°, 8.3°, and 7.7° for the as-grown, 2.3 V, and 1.5 V films, respectively. Here, we note that FWHM (=7.9°) of
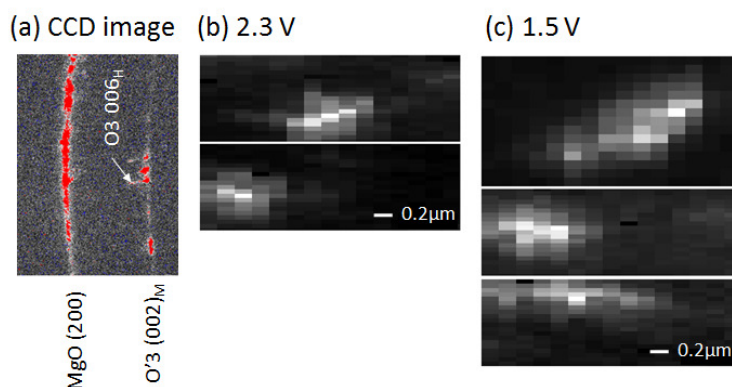
the fully-charged $Na_{0.5}CoO_2$ film is comparable to those of the 2.3 V and 1.5 V films. This indicates that the increase in FWHM should be ascribed to the initial charge process, and not to the subsequent discharge process. This means that the initial charge process enlarges the out-of-plane distribution of the crystal orientation.

Figure 2. (**a**) X-ray diffraction (XRD) pattern of the as-grown, 2.3 V, and 1.5 V films. Values in parentheses represent indexes in the trigonal [hexagonal (H) setting] and monoclinic (M) structures. (**b**) rocking curve at the 003_H, 001_M, and 001_M reflections of the as-grown, 2.3 V, and 1.5 V films, respectively. Solid curves are results of the least-squares fittings with Gauss functions.

2.3. X-Ray Microdiffraction

Figure 3a shows an example of the charge coupled device (CCD) image of the 2.3 V film at $2\theta \sim 33°$. We observed many Bragg reflections, indicating that there exists many crystal domains in the footprint area (1130 nm (H) × 260 nm (V)) of the incident X-ray. We found that most of the spots are ascribed to the O′3 phase. This indicates that the 2.3 V film is dominated by the O′3 phase, consistent with the XRD pattern of the 2.3 V film (Figure 2a). Thus, we concentrated our attention on the *r* values of the respective O′3 domains. We measured the intensity images (XRMD images) of specific Bragg spots against the sample position (x, y) relative to the incident X-ray.

Figure 3. (**a**) Example of the charge coupled device (CCD) image of the 2.3 V film at $2\theta \sim 33°$. The footprint area of the incident X-ray was 1130 nm (H) × 260 nm (V). (**b**) X-ray microdiffraction (XRMD) images of O′3 domains of the 2.3 V film; and (**c**) XRMD images of O′3 domains of the 1.5 V film.

Figure 3b shows examples of the XRMD images of the O′3 domains in the 2.3 V film. The images are *x*-elongated due to the worse horizontal resolution (=1130 nm). Therefore, we evaluated the domain

sizes along the *y*-direction by means of least-squares fitting with a Gauss function. The *r* values are 365 nm (upper image in Figure 3b) and 357 nm (lower). We performed similar analyses in the 1.5 V film and evaluated the sizes of the O′3 domains (Figure 3c). The *r* values are 331 nm (upper image in Figure 3c), 431 nm (middle), and 571 nm (lower). Thus-obtained domain size *r* ($\approx$400 nm) is comparable to the particle size *d* (=331 $\pm$ 87 nm) in the as-grown film. This observation suggests that individual particles of Na_xCoO_2 are single phase.

3. Discussion

Here, let us discuss the mechanism of the PS in $O3\text{-}NaCoO_2$. In Na_xCoO_2, the high- and low-*x* regions prefer the O3 and O′3 structures, respectively [7]. Then, the Na^+ deintercalation can trigger the PS. For convenience of explanation, we classify the PS into two types: microscopic PS within the particle, and macroscopic PS between the particles. The microscopic PS is initiated by nucleation of the second (O′3) phase, whose size is determined by the balance between the free energy gain due to the phase transformation and the strain loss at the O3–O′3 phase boundaries. The microscopic PS, however, suffers from the inner stresses at the phase boundaries. On the other hand, the macroscopic PS is energetically advantageous because homogeneity of the particle structure releases the inner stresses. This scenario is analogous to the domino-cascade model proposed in Li_xFePO_4 [10]. We note that macroscopic phase separation into high- and low-*x* regions is possible in battery materials, because the local charge neutrality is kept by the oxidation of the transition metal.

Our XRMD investigation suggests that individual particles of Na_xCoO_2 are single phase. In other words, Na_xCoO_2 shows macroscopic PS in the O3–O′3 two-phase region. Then, the charge process of $O3\text{-}NaCoO_2$ is considered to be as follows. The Na^+ deintercalation causes the formation of a O′3 micro-domain within the O3 particle. The O3–O′3 phase boundary is energetically unstable, because the cell parameters are significantly different between the O3 and O′3 phases: *a* = 2.8883 Å and *c* = 15.6019 Å in $NaCoO_2$ (O3) while *a* = 4.8912 Å, *b* = 2.8681 Å, *c* = 5.7927 Å, and β = 111.84° in $Na_{0.83}CoO_2$ (O′3) [7]. In addition, the *c* axis tilts toward the *a* axis by 21.84° in the O3′ phase, even though the oxygen stacking is the same as in the O3 phase. Such a tilting is also responsible for the instability of the O3–O′3 phase boundary. Then, the O3–O′3 phase boundaries behave as active sites for the electrochemical reaction. This is because the Na^+ deintercalation at the phase boundary is much easier than the nucleation of a new O′3 micro-domain in another particle. After the competition of the O3–O′3 transformation in one particle, formation of another O′3 micro-domain takes place in another O3 particle.
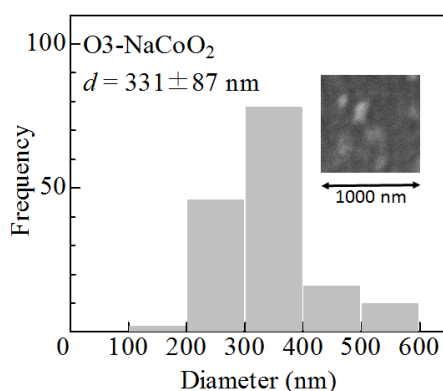
4. Materials and Methods

4.1. Film Preparation and Characterization

A thin film of $O3\text{-}NaCoO_2$ was prepared by pulsed laser deposition (PLD) method [9]. The film was grown on Au-deposited MgO (100) substrate at 823 K in an oxygen partial pressure of 0.01 Pa for 20 min. The area of the film was $0.5\ cm^2$. The targets of $O3\text{-}NaCoO_2$ were prepared by solid state reaction. First, Na_2O_2 and Co_3O_4 were mixed in a 1.25:1.0 atomic ratio and calcined at 823 K for 16 h in O_2 atmosphere. Then, the powder was finely ground, pressed into pellets with 10 mm diameter, and calcined at 823 K for 16 h in O_2 atmosphere. The second harmonics of an yttrium–aluminum–garnet (YAG) pulse laser was used as excitation light source. The pulse energy, repetition frequency, and wavelength were $2.0\ J/cm^2$, 10 Hz, and 532 nm, respectively. The distance between the target and the substrate was 35 mm. The XRD pattern indicates the O3 structure, which is stable in a narrow *x*-range (0.99 $\leqslant$ *x* $\leqslant$ 1) [7]. Therefore, we regard the chemical composition of the film as $NaCoO_2$.

The morphology of the as-grown film was investigated using scanning electron microscopy (SEM) images (Mighty-8, TECHNEX, Tokyo, Japan). The acceleration voltage was 2 keV. The as-grown film of $O3\text{-}NaCoO_2$ consists of crystalline particles. The particle size *d* (=331 $\pm$ 87 nm) was evaluated from 152 particles (Figure 4). The film thickness (*L*) was 250 nm, which was determined by cross-sectional

SEM image. The mass (=0.063 μg) of the active material was estimated by L and the ideal density (=5.02 g/cm^3) of $NaCoO_2$.

Figure 4. Histogram of the particle size (d) of the as-grown O3-$NaCoO_2$ film. Inset shows scanning electron microscopy (SEM) images of the film.

4.2. Control of x

The x values were electrochemically controlled in the discharge process from the fully-charged $Na_{0.5}CoO_2$ film in a handmade two-pole cell. The cathode and anode were the film and the Na metal, respectively. The electrolyte was propylene carbonate (PC) containing 1 M $NaClO_4$. The upper cut-off voltage was 3.8 V. The charge/discharge rate was ~1 C. The discharge capacity (=112 mAh/g) was close to the ideal value (=113 mAh/g) of O3-$NaCoO_2$. We cut the as-grown O3-$NaCoO_2$ film into four pieces. After the charge process, we performed a discharge run, setting the lower cut-off voltage at 1.5 V (1.5 V film) or 2.3 V (2.3 V film). In the XRD and rocking curve measurements, we used a set of films prepared from the same film. In the scanning X-ray microbeam diffraction, we used another set of films.
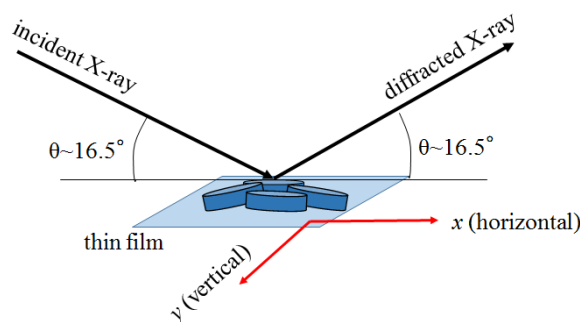
4.3. X-Ray Diffraction and Rocking Curve

The XRD patterns were obtained using an X-ray powder diffractometer (MultiFlex, Rigaku, Tokyo, Japan) with the Bragg–Brentano (θ–2θ) geometry. The X-ray source was the Cu Kα line (λ = 1.54 Å) operated at 40 kV and 40 mA. A Si monochromator was used to reduce the scattering by the white X-ray. The rocking curve was measured at the 003_H, 001_M, and 001_M reflections of the as-grown, 2.3 V, and 1.5 V films, respectively. In the measurement, the θ axis was scanned fixing 2θ at the peak position of the reflection.

4.4. X-Ray Microdiffraction

XRMD experiments were performed using a hard X-ray undulator beamline (BL13XU) at SPring-8 [11,12]. The X-ray energy (E) was 8 keV. The energy resolution ($\Delta E/E$) was 10^{-4} using a Si(111) double-crystal monochromator. The wavelength of the incident X-ray microbeam was 1.55 Å. The size of the incident X-ray microbeam was 330 nm (H) × 260 (V) nm using a zone plate.

Figure 5 shows a schematic configuration of the XRMD experiment. The X-ray microbeams are incident at an angle of θ ~ 16.5°, which corresponds to the 006_H reflection of the O3 phase and 002_M reflection of the O′3 phase. The penetration depth is 11.3 μm at 8 keV. The diffracted X-ray microbeam was acquired with a CCD. We measured the CCD image of the diffraction intensity against the relative position (x, y) of the X-ray microbeam. Focusing on a certain domain, we obtained the real-space mapping (XRMD image) of the diffraction intensity within region of interest (ROI) in the CCD image. In this diffraction geometry, the footprint area of the incident X-ray was 1130 nm (H) × 260 nm (V) on

the film surface. Therefore, the x-resolution (=1130 nm) is much worse than the y-resolution (=260 nm). The intervals of x and y were 200 nm and 50 nm, respectively.

Figure 5. Schematic configuration of XRMD.

5. Conclusions

We performed XRMD investigation on the $(001)_M$ reflections of a thin film of Na_xCoO_2 in the O3–O′3 two-phase region. We found that r ($\approx$400 nm) of the O′3 domain is comparable to the particle size d (=331 $\pm$ 87 nm) in the as-grown O3-$NaCoO_2$ film. This observation suggests that Na_xCoO_2 shows the macroscopic PS in the O3–O′3 two-phase region. We discussed the charge process of O3-$NaCoO_2$ in terms of the O3–O′3 phase boundaries as active sites.

Author Contributions: Hideharu Niwa performed all the experiments including the film preparation and characterization, and X-ray microdiffraction measurements. Takayuki Shibata provided advices regarding the film preparation and characterization. Yasuhiko Imai and Shigeru Kimura collaborated in the X-ray microdiffraction measurements as beamline staff. Yutaka Moritomo planned the research and wrote the manuscript.

Conflicts of Interest: The authors declare no conflict of interest.

References

1. Kim, S.-W.; Seo, D.-H.; Ma, X.; Ceder, G.; Kang, K. Electrode materials for rechargeable sodium-ion batteries: Potential alternatives to current lithium-ion batteries. *Adv. Energy Mater.* **2012**, *22*, 710–721.
2. Ong, S.-P.; Chevrier, V.-L.; Hautier, G.; Jain, A.; Moore, C.; Kim, S.; Ma, X.; Ceder, G. Voltage, stability and diffusion barrier differences between sodium-ion and lithium-ion intercalation materials. *Energy Environ. Sci.* **2011**, *4*, 3680–3688.
3. Komaba, S.; Murata, W.; Ishikawa, T.; Yabuuchi, N.; Ozeki, T.; Nakayama, T.; Ogata, A.; Gotoh, K.; Fujiwara, K. Electrochemical Na insertion and solid electrolyte interphase for hard-carbon electrodes and application to Na-ion batteries. *Adv. Energy Mater.* **2011**, *21*, 3859–3867.
4. Komaba, S.; Takei, C.; Nakayama, T.; Ogata, A.; Yabuuchi, N. Electrochemical intercalation activity of layered $NaCrO_2$ vs. $LiCrO_2$. *Electrochem. Commun.* **2010**, *12*, 355–358.
5. Yoshida, H.; Yabuuchi, N.; Komaba, S. $NaFe_{0.5}Co_{0.5}O_2$ as high energy and power positive electrode for Na-ion batteries. *Electrochem. Commun.* **2013**, *34*, 60–63.
6. Zhao, K.; Zhao, L.; Dimov, N.; Okada, S.; Nishida, T. Electrochemical and thermal properties of α-$NaFeO_2$ cathode for Na-ion batteries. *J. Electrochem. Soc.* **2013**, *160*, A3077–A3081.
7. Lei, Y.; Li, X.; Liu, L.; Ceder, G. Synthesis and stoichiometry of different layered sodium cobalt oxides. *Chem. Mater.* **2014**, *26*, 5288–5296.
8. Delmas, C.; Braconnier, J.; Fouassier, C.; Hagenmuller, P. Electrochemical intercalation of sodium in Na_xCoO_2 bronzes. *Solid State Ion.* **1981**, *3–4*, 165–169.

9.　Shibata, T.; Fukuzumi, Y.; Kaboyashi, W.; Moritomo, Y. Fast discharge process of layered cobalt oxides due to high Na^+ diffusion. *Sci. Rep.* **2015**, *5*, doi:10.1038/srep09006.

10.　Delmas, C.; Maccario, M.; Croguennec, L.; Le Cras, F.; Weill, F. Lithium deintercalation in $LiFePO_4$ nanoparticles via a domino-cascade model. *Nat. Mater.* **2008**, *7*, 665–671.

11.　Imai, Y.; Kimura, S.; Sakata, O.; Sakai, A. High-angular-resolution microbeam X-ray diffraction with CCD detector. *AIP Conf. Proc.* **2010**, *1221*, 30–32.

12.　Takeda, S.; Kimura, S.; Skata, O.; Sakai, A. Development of high-angular-resolution microdiffraction system for reciprocal space map measurement. *Jpn. J. Appl. Phys.* **2006**, *45*, L1054–L1056.